Available online at www.sciencedirect.com

ScienceDirect

Procedia IUTAM 26 (2018) 174–183

Procedia IUTAM

www.elsevier.com/locate/procedia

IUTAM Symposium Wind Waves, 4-8 September 2017, London, UK

Impacts of wave age on turbulent flow and drag of steep waves

Peter P. Sullivan[a,*], Michael L. Banner[b], Russel P. Morison[b], William L. Peirson[c]

[a]*National Center for Atmospheric Research, Boulder, Colorado, USA*
[b]*School of Mathematics and Statistics, The University of New South Wales, Australia*
[c]*New College, The University of New South Wales, Australia*

Abstract

Turbulent flow over steep steady and unsteady wave trains with varying height $h(x,t)$ and propagation speed c is simulated using large-eddy simulation (LES) in a wind-wave channel [17]. The imposed waveshape with steady wave trains is based on measurements of incipient and active breaking waves collected in a wind-wave tank, while a numerical wave code is used to generate an unsteady evolving wave train (or group) [3]. For the adopted waveshapes, process studies are carried out varying the wave age c/u_* from ~ 1 to 10: the airflow friction velocity is u_*. Under strong wind forcing or low wave age $c/u_* \sim 1$, highly intermittent airflow separation is found in all simulations and the results suggest separation near a wave crest occurs prior to the onset of wave breaking. As wave age increases flow separation is delayed or erased for both steady and unsteady wave trains. Flow visualization shows that near the wave surface vertical velocity w and waveslope $\partial h/\partial x$ are positively correlated at $c/u_* \sim 1$ but are negatively correlated at $c/u_* = 10$. The vertical speed of the underlying wave oscillations depends on the local waveslope, increases with phase speed, and is a maximum on the leeward side of the wave. Vigorous boundary movement [8] appears to alter the unsteady flow separation patterns which leads to a reduction in form (pressure) drag as wave age increases. For example, the pressure contribution to the total drag of the active breaker wave train decreases from 74% at $c/u_* = 1.23$ to less than 20% at $c/u_* = 10$. Critical layer dynamics appears to play a secondary role in the air-wave coupling over steep waves, but requires further investigation. For all simulations, the form drag is found to be strongly dependent on both waveslope $\partial h/\partial x$ and wave age c/u_*. The simulations are in good agreement with experimental results for turbulent flow over steep waves under strong wind forcing.

© 2018 The Authors. Published by Elsevier B.V.
Peer-review under responsibility of the scientific committee of the IUTAM Symposium Wind Waves.

Keywords: turbulence ; water waves ; unsteady separation ; drag ; wave age

1. Introduction

Air-sea interaction fluxes of fundamental scalar and dynamical variables couple the atmosphere and the ocean, and are crucial for short and long term environmental forecasting. Yet, despite decades of intensive research, there remain significant knowledge gaps in the underlying physical processes that need to be resolved in order to improve forecast accuracy for applications ranging from mesoscale to climatic time scales. Wind waves underpin key air-sea interfacial

* Corresponding author. Tel.: +1-303-497-8953 ; fax: +1-303-497-8171.
E-mail address: pps@ucar.edu

2210-9838 © 2018 The Authors. Published by Elsevier B.V.
Peer-review under responsibility of the scientific committee of the IUTAM Symposium Wind Waves.
10.1016/j.piutam.2018.03.017

exchange processes across the wind-driven sea surface, especially under strong wind forcing. Which wind-wave scales and transfer mechanisms are operative, and under what circumstances are they significant, or even dominant? These questions motivate our simulation study, which focuses on very strongly-forced wave scales and the impact of the wave steepness, wave age and modulational variability of the surface geometry on the interfacial dynamics and scalar fluxes. The role of strongly forced (steep) waves in coupling turbulent winds to the ocean surface and currents is not well understood at a fundamental level because of the inherent nonlinear and dissipative fluid dynamics.

In order to shed light on air-water coupling mechanics for steep waves we recently carried out an investigation of turbulent flow above steady and unsteady wave trains using large eddy simulation (LES) [17]. To carry out the process studies a highly idealized simulation design was adopted: The steep waves imposed at the lower boundary of the LES are synthesized shapes measured in a wind-wave tank [2]. The observed waves are not monochromatic, but feature sharp crests with shallow troughs and local waveslopes $\partial h/\partial x$ that are asymmetrical about the wave crest; $-\partial h/\partial x$ is noticeably larger forward of a wave crest. The waves are near or slightly past the onset of full breaking with spilling fluid down the face of the wave. Also, we examine the impact of modulational variability of the surface by imposing a time and space varying wave packet (group) [3] at the LES lower boundary. In all the simulations, the wave age $c/u_* \sim 1$, where c is the characteristic phase speed of the wave and u_* is the air friction velocity.

The major findings from [17] are: 1) highly intermittent airflow separation is observed and occurs before the onset of full breaking; 2) the form (pressure) drag increases markedly as the waves cross the boundary from incipient to active breaking; 3) the LES results are in good agreement with experimental observations; and 4) intermittent separation is found in flow over the wave packet, and its form drag is well correlated with the evolving waveslope. The goal of the present work is to expand our process studies and examine the impact of increasing wave age on winds and surface drag for steep steady and unsteady wave trains. The simulation design is identical to that described in [17], but now with varying c/u_*.

Nomenclature

ak	root-mean-square (rms) waveslope
c	wave phase speed
c/u_*	wave age
e	subgrid scale energy
$h(x,t)$	wave height
$\partial h/\partial x$	local waveslope
h_{cr}	height of critical layer
J	Jacobian of the grid transformation
(L_x, L_y, H)	dimensions of computational box
(N_x, N_y, N_z)	gridpoints used to discretize (L_x, L_y, L_z)
$\partial\mathcal{P}/\partial x$	imposed pressure gradient
k	wavenumber $= 2\pi/\lambda$
p	static pressure
t	time
$\mathbf{u}$	Cartesian velocity vector $u_i = (u, v, w)$
u_*	surface friction velocity
w_o	vertical velocity of the wave surface
$\mathbf{x}$	Cartesian coordinates $x_i = (x, y, z)$
z_o	surface roughness
z_t	translation speed of vertical gridlines (grid speed)
λ	wavelength
ν_t	subgrid scale eddy viscosity
$\boldsymbol{\xi}$	computational coordinates $\xi_i = (\xi, \eta, \zeta)$
ϖ	stretching factor in grid generation
ρ	air density

τ_{ij}	subgrid scale stress tensor
$\langle f \rangle$	space-time average of f at constant ζ and over t
$[f]$	spanwise y average of f at constant x
$(f)'$	turbulent fluctuation
	(velocity, length, time) are dimensionless by $(u_*, \lambda, \lambda/u_*)$

2. Large-eddy simulation

2.1. Large-eddy simulation

An overview of the LES model is presented here in order to introduce the coordinate system, variables, and the basics of the solution algorithm [21, 10, 17]. The following nomenclature is used: $\mathbf{u} \equiv u_i = (u, v, w)$ denote the Cartesian velocity components and p is the pressure variable normalized by density ρ. The three Cartesian coordinates are $\mathbf{x} \equiv x_i = (x, y, z)$ which are also referred to as (streamwise, spanwise, vertical) directions, respectively, and t is time.

We simulate incompressible turbulent boundary-layer flow in a channel with a flat upper boundary and a wavy moving lower boundary. Then the set of spatially filtered LES equations that describe the flow are:

$$\frac{\partial u_i}{\partial x_i} = 0\,, \tag{1}$$

$$\frac{\partial u_i}{\partial t} = -\frac{\partial u_j u_i}{\partial x_j} - \frac{\partial p}{\partial x_i} - \frac{\partial \tau_{ij}}{\partial x_j} - \frac{\partial \mathcal{P}}{\partial x_i}\delta_{i1} \tag{2}$$

The boundary-layer winds are driven by a large-scale imposed external streamwise pressure gradient $\partial\mathcal{P}/\partial x$ that is constant in space and time. To enforce mass conservation the pressure variable p is determined from an elliptic Poisson pressure equation $\nabla^2 p = \mathcal{R}$ formed by applying the discrete divergence operator to the velocity time tendencies, $\nabla \cdot (\partial_t \mathbf{u})$. To close the system of equations the subgrid-scale (SGS) momentum flux τ_{ij} requires modeling in the interior of the flow and at the lower boundary. We use an eddy viscosity prescription $\nu_t \sim \sqrt{e}$ where e is the subgrid-scale kinetic energy. An additional transport equation for SGS energy e is added to the LES equation set (1, 2). The molecular Reynolds number is assumed to be high and molecular diffusion terms are neglected in (2).

2.2. Coordinate transformation

The LES code integrates the governing equations (1, 2) in a time varying non-orthogonal surface following coordinate system. The computational coordinates are $\xi_i = (\xi, \eta, \zeta)$, and the wave-following grid transformation and metrics that map physical space to computational space $(x, y, z, t) \Longleftrightarrow (\xi, \eta, \zeta, t)$ are

$$\begin{aligned} &x = \xi, \quad y = \eta, \quad z = \zeta + h(x,t)\left(1 - \frac{\zeta}{H}\right)^{\varpi}, \\ &\xi_x = 1, \quad \zeta_x = -z_\xi J, \quad \zeta_z = 1/z_\zeta = J, \quad z_t = -\zeta_t/J\,. \end{aligned} \tag{3}$$

The imposed time varying surface wave height is $h(x, t)$ and the top of the computational domain is H. The Jacobian of the mapping transformation $J = \partial\zeta/\partial z$, and the vertical coordinate lines move up and down with grid speed $z_t \equiv \partial z/\partial t = -(\partial\zeta/\partial t)/J$. The slope of a wave following streamwise gridline is $z_\xi \equiv \partial z/\partial\xi = -(\partial\zeta/\partial x)/J$. Parameter $\varpi = 3$ controls how rapidly the streamwise gridlines become level surfaces with increasing distance from the surface in physical space. The transformation (3) is a smooth single valued function and produces continuous spatial derivatives $\partial\xi_i/\partial x_j$ and time derivatives $\partial\xi_i/\partial t$. The mapping allows an arbitrary waveform to be imposed at the lower boundary with the gridlines translating vertically so as to follow the moving wave.

The governing equations, in transformed coordinates, are discretized in strong conservation flux form using the volume flux or "contravariant flux" velocities positioned at the cell faces of a computational stencil. The Cartesian velocity components, pressure, SGS energy are then conveniently co-located at the center of the stencil. The spatial

differencing is pseudospectral in the (ξ, η) directions and second-order finite difference in the ζ direction. A dynamic time step is used in combination with the third-order Runge-Kutta time integration.

2.3. Simulations

All simulations are performed in non-dimensional units with (length, velocity, time) scales made dimensionless by (wavelength λ, friction velocity u_*, time scale λ/u_*). At the wavy surface, the LES applies wall functions at every (ξ, η) gridpoint assuming a non-dimensional surface roughness $z_{o,s} = 4.3 \cdot 10^{-4}$.

For the simulations of airflow over steady wave trains, the computational domain is $(L_x, L_y, H) = (5, 5, 1)$ and the discretization employs $(N_x, N_y, N_z) = (512, 512, 128)$ gridpoints. Equally spaced grids are used in the horizontal directions while a smoothly stretched mesh is used in the vertical direction with spacing $\zeta_1 = 0.0065$ at the first grid level off the water surface. The wave height $h(x, t)$ imposed at the lower boundary of the LES is a synthesized waveshape observed in a wind-wave tank by Banner [2]. Two types of steep steady waves are considered, *viz.,* waves near the onset of breaking and waves with spilling flow down the forward face of the wave: in the following discussion they are referred to as "incipient" and "active" breaking, respectively. The steady wave trains are assumed to propagate in time with the dominant phase speed c observed in the experiments. The simulations are initiated with turbulent fields archived from a slightly heated surface.

Under steady conditions, the LES equations obey an integral momentum flux balance given by

$$-\frac{\partial \mathcal{P}}{\partial x} H \equiv u_*^2 = -\left\langle \frac{p}{J}\frac{\partial \zeta}{\partial x} + \frac{\tau_{1k}}{J}\frac{\partial \zeta}{\partial x_k} \right\rangle \Bigg|_{\zeta=0} . \tag{4}$$

In the above, angle brackets $\langle\ \rangle$ denote an ensemble space-time average, the spatial averaging is along wave-following (ξ, η) surfaces at constant ζ. As expected (4) shows that the large scale pressure gradient is balanced by a surface drag which is a combination of form and viscous drag. The simulations of steady wave trains are carried out for more than 200,000 timesteps until the time and space varying drag of the underlying wave surface, given by (4), reaches a statistically steady state.

Also, we simulate turbulent flow over an unsteady evolving wave group or chirp packet in the domain $(L_x, L_y, H) = (9.40, 4.695, 1)$ discretized using $(N_x, N_y, N_z) = (1024, 512, 128)$ mesh points. The space-time evolving height $h(x, t)$ of the wave packet is generated by a fully nonlinear wave tank code. A special recipe utilizing fully developed turbulent boundary-layer flow over a flat boundary, described in [17], is used to compute flow over the unsteady wave packet.

Previously, we carried out simulations of both steady and unsteady wave trains under strongly forced conditions with wave age $c/u_* \sim 1$. The focus of the present work is to expand the simulation parameter space and examine the impact of wave age on the airflow and surface drag for steep more rapidly propagating surface waves. Thus, as a first approximation, we simply adopt the same wave height distributions as in [17] but increase the wave age to larger values $c/u_* = (5, 10)$. The LES solutions are obtained using non-dimensional variables and thus increases in wave age can be interpreted as a change in wind speed or wave scale (or a combination of the two) in physical units. For example, for the incipient breaker $c/u_* = 10$ approximately corresponds to either a factor 6 reduction in the surface wind speed or a factor 40 increment in the wavelength λ compared to $c/u_* = 1.58$. Note that values of $c/u_* = (5, 10)$ still represent young (growing) seas compared to wind-wave equilibrium $c/u_* \sim 25 - 30$ [1].

3. Interpretation of results

Inspection of the instantaneous flow fields and low-order statistical moments shows wave age significantly impacts turbulent flow over steep steady and unsteady wave trains. Broadly, we find that wave age and waveslope both significantly impact the velocity and pressure fields, and hence surface drag.

3.1. Flow visualization

A particularly sensitive metric that highlights the wave age dependence is vertical velocity w, furthermore w has the favorable property that it is invariant when viewed in a stationary or horizontally translating frame of reference. Figure 1 shows contours of y (or phase) averaged vertical velocity $[w]$ in a zoom over a limited $x - z$ area for the

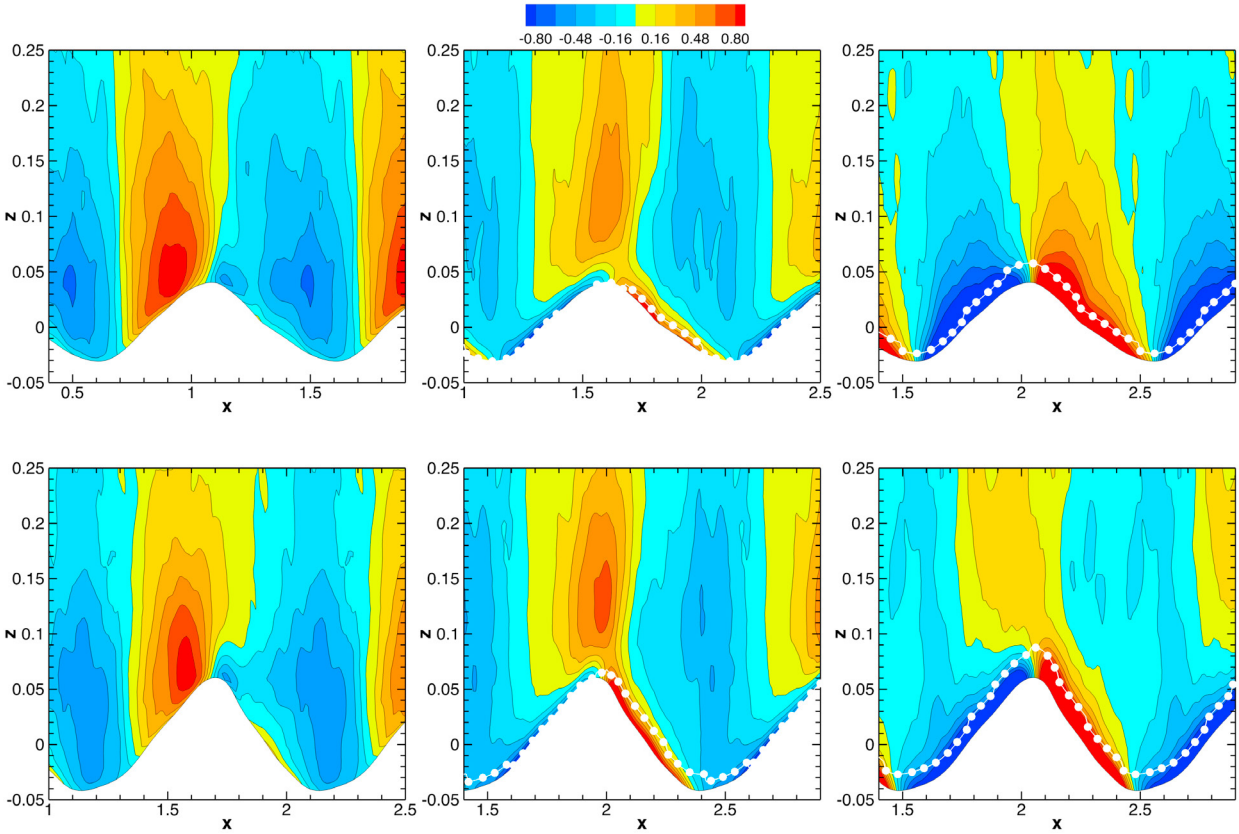

Fig. 1. Contours of y averaged vertical velocity $[w]$ normalized by u_*. Top row, train of incipient breakers with varying wave age, $c/u_* = (1.58, 5, 10)$ (left, middle, right) panels, respectively. Bottom row, train of active breakers with varying wave age, $c/u_* = (1.23, 5, 10)$ (left, middle, right) panels, respectively. The height of the critical layer h_{cr} for simulations with wave age $c/u_* = (5, 10)$ is indicated by the white bullets. Note, for smaller wave age h_{cr} is collapsed down to the wave surface and is not shown. The color bar is held constant between the images. The wind and wave propagation direction is left to right in all cases.

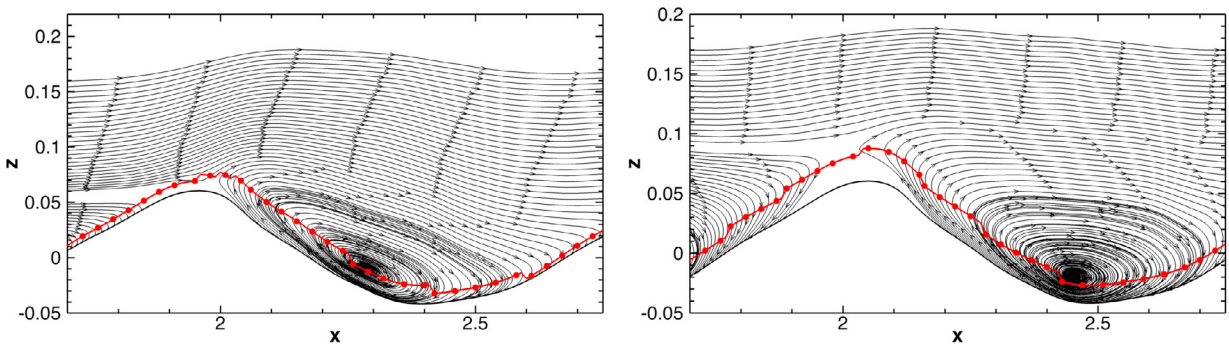

Fig. 2. Phase average streamlines for a train of active breakers in a frame of reference moving with the wave phase speed c. (Left, right) panels $c/u_* = (5, 10)$, respectively. The red line denotes the critical layer height h_{cr}, as shown and computed in Fig. 1.

incipient and active breakers for three values of wave age. Each image displays small random fluctuations because of limited sampling, only a single 3-D volume is used to construct the y average. Systematic pattern shifts with varying c/u_* are however clearly discernible. At small wave age $c/u_* = O(1)$, (positive, negative) vertical velocity is correlated

with (positive, negative) waveslope as expected for slow moving strongly forced waves. In the wave trough, the phase averaged vertical velocity is negative and weak in magnitude, a consequence of the slow rotational motions in the intermittent flow separation zones that develop on the leeward side of steep waves [22, 15, 5, 17]. Notice as wave age increases $c/u_* = (5, 10)$, waveslope and vertical velocity become negatively correlated. At $c/u_* = 10$, for both incipient and active breakers, near surface $[w] > 0$ is correlated with $\partial h/\partial x < 0$, while $[w] < 0$ is correlated with $\partial h/\partial x > 0$. Most importantly these pattern shifts in $[w]$ are also found to coincide with an overall change in the flow separation dynamics for steep waves. Visualization indicates the flow separation observed at low wave age (left panels of Fig. 1) is delayed or erased with increasing wave age – the reduction in flow separation produces a significant impact on the surface pressure and drag of the underlying wavy surface as discussed in section 3.2. At wave age $c/u_* = 5$ an elevated maximum in $[w]$ is also observed well above the wave crest with a thin pocket of positive $[w]$ developing on the leeward face of the wave. The near discontinuous phase jump in w with increasing distance from the wave surface resembles the flow pattern induced by critical layers in direct numerical simulations of turbulent flow over low slope monochromatic waves, see Figs. 18 and 19 in [20], and in observations [11, 9].

Our initial speculation is that the shifting w patterns are a result of critical layer dynamics [12] which emerge with increasing c/u_*. To explore this possibility, the vertical velocity contours in Fig. 1 are overlaid with the local critical layer height h_{cr} computed from the phase average relation $[u(x, z)] = c$. Examination of the curves in all cases shows $h_{cr}(x, z)$ remains tightly confined to the wave surface $h(x, t)$ irrespective of wave age. For example, in Fig. 1 for the highest wave age considered $c/u_* = 10$ at location $x = 2.05$, the vertical separation between the wave and critical layer heights is narrow $(h, h_{cr}) = (0.058, 0.087)$ for the active breaker. The small surface roughness imposed in the LES $z_{o,s} = 4.3 \cdot 10^{-4}$ further collapses the height of the critical layer towards the water surface (see p. 128 of [14] and [4]). A characteristic signature of a critical layer is a closed pattern of streamlines or cat's-eye when viewed in a frame of reference moving with the wave phase speed c [4]. Figure 2 depicts streamlines computed from the phase average vector $([u] - c, [w])$ for the active breaker at two values of wave age. The streamlines are closed but vertically very distorted. The tightly wound center of the cat's-eye is compacted very near the wave surface and its position is slightly upstream of the wave trough. Overall, the shape of the cat's-eye pattern with nonlinear steep waves and turbulence is noticeably different than its theoretical counterpart with low-turbulence stresses and small wave amplitude [4, 16].

Although the critical layer in Fig. 2 potentially plays a role in the air-wave coupling for steep waves, the observed changes in the near surface vertical velocity and separation flow patterns, and surface drag appear to be more closely associated with a wave driving (or boundary pumping) effect that increases with phase speed c. To diagnose the magnitude of the boundary pumping consider the locally varying waveslope of the steep 2-D wave trains in Fig. 1. The lower boundary condition in the simulations imposes no net flow across the wave surface, but the wave boundary temporally and spatially oscillates. Its vertical velocity w_o is approximately given by (see, equation 8 in [17])

$$w_o \sim \frac{\partial h}{\partial t} = -c\frac{\partial h}{\partial x} \tag{5}$$

Thus, boundary movement can generate large (positive, negative) near surface vertical velocities in regions with large (negative, positive) waveslope depending on the phase speed. Since the maximum waveslope $-\partial h/\partial x = (0.25, 0.4)$ for (incipient, active) breakers, respectively, large w and $[w] > 0$ are generated on the leeward side of a wave as shown in the right panels of Fig. 1. In other words, for large wave age near surface $[w]$ and $\partial h/\partial x$ are negatively correlated. The surface boundary pumping velocity $w_o \sim c$ and increases by more than a factor of 6 for $c/u_* = 10$ compared to the strongly forced waves with $c/u_* \sim O(1)$. Because the spatially varying boundary pumping is maximum forward of a wave crest it has the potential to alter flow separation. Analysis of the vertical velocity flowfields for an unsteady chirp packet exhibit similar patterns when the wave age is increased by a factor of 10.

3.2. Pressure, form drag, and velocity profiles

Wave age also leaves a clear imprint on the instantaneous surface pressure and its correlation with waveslope (see Fig. 3), the form drag (see Fig. 4), and the mean velocity profiles (see Fig. 5). For example, the incipient case with $c/u_* = 1.58$, left panel of Fig. 3, features intermittent flow separation zones when viewed in an $x - y$ plane with spatially episodic values of $(p\partial h/\partial x)/u_*^2 > 5$. As c/u_* increases from 1.58 to 5 the fluctuations in the pressure-waveslope correlation decrease considerably, and $|p\partial h/\partial x|/u_*^2 < 2$ over the entire horizontal domain at $c/u_* = 10$ (not shown). The waveshape is held constant in the simulations as c/u_* varies, and then the reduced pressure-waveslope

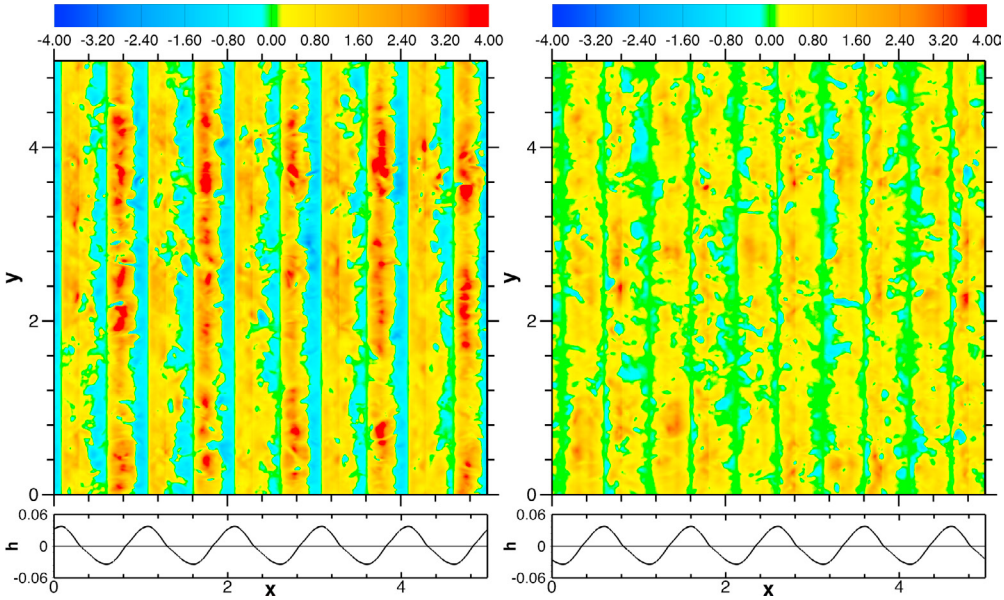

Fig. 3. Pressure waveslope correlation $p\partial h/\partial x$ normalized by u_*^2 for varying wave age, $c/u_* = (1.58, 5)$ (left, right) panels, respectively. The color bar is held constant between the two images. The instantaneous wave height $h(x,t)$ corresponding to each case is shown in the bottom panels. The wind and wave propagation direction is left to right.

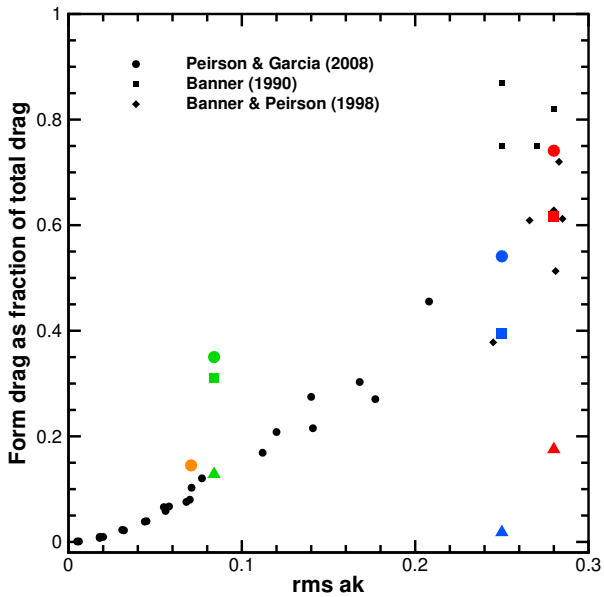

Fig. 4. Form (pressure) drag for LES cases with steady and unsteady waves for varying rms waveslope and wave age. Incipient case with rms $ak = 0.25$, $c/u_* = (1.58\ \bullet, 5\ \blacksquare, 10\ \blacktriangle)$; Active case with rms $ak = 0.28$, $c/u_* = (1.23\ \bullet, 5\ \blacksquare, 10\ \blacktriangle)$; No breaking case with rms $ak = 0.071$, $c/u_* = (1\ \bullet)$; Unsteady wave packet with rms $ak = 0.084$, $c/u_* = (1\ \bullet, 5\ \blacksquare, 10\ \blacktriangle)$. Black symbols are laboratory measurements with wave age $c/u_* = O(1)$.

correlations in the right panel of Fig. 3 primarily result from a lower magnitude of fluctuating surface pressure p; small phase shifts in the surface pressure relative to the waveshape play a secondary role. Similar changes are also found in the simulations with active breakers and unsteady chirp packets.

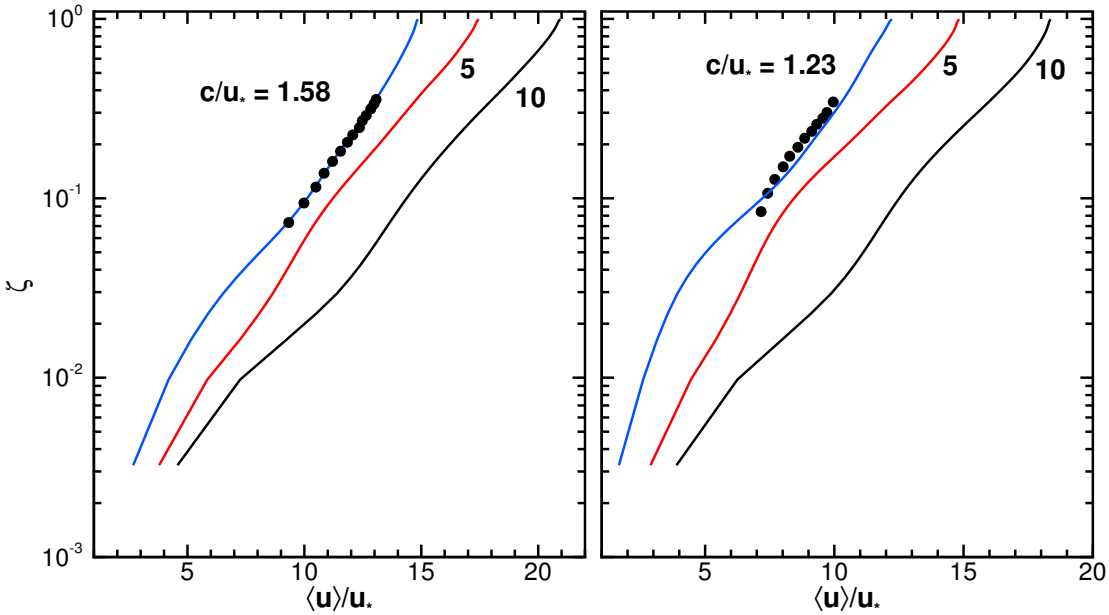

Fig. 5. Vertical wind profiles $\langle u \rangle / u_*$ over (incipient, active) breaking waves (left, right) panels. Measurements from Banner (1990) [2] are indicated by •.

Figure 4 summarizes the form drag variation (or more precisely the ratio of form drag to the total drag, *i.e.,* the form drag fraction) for different combinations of rms waveslope and wave age. Results are obtained by space-time averaging the pressure-waveslope correlations. As anticipated based on the findings in Fig. 3, for a given waveform of fixed steepness the form drag noticeably decreases with increasing wave age. For the active breaker, the form drag fraction decreases from 74% to 17.5% for an increase in wave age from 1.23 to 10. The variability of the wave surface geometry, in terms of amplitude and tilt modulation, is also found to have a substantial effect on the flow separation and hence on the form drag, for very young wave age conditions. This is seen in Fig. 4 when comparing the green and orange symbols for an rms steepness of ~ 0.08 and $c/u_* \sim 1$. The modulational effects are seen to result in a near-doubling of the form drag, see [17].

Thus, form drag is a strong function of at least two-parameters, *viz.,* waveslope and wave age. Simulations of steep waves with increasing wave age produce a surface drag reduction somewhat analogous to swell in the open ocean. In swell-wave driven wind scenarios the form drag can be negative, *i.e.,* upward from the ocean to the atmosphere under light wind conditions. However, remotely generated swell is typically characterized by wave age $c/u_* > 30$, low waveslope $ak < 0.1$ [7, 18, 19], and no flow separation in contrast to the steep waves considered here. The underlying dynamics that lead to a form drag reduction with rapidly moving steep waves appears to be fundamentally different than wind-swell coupling.

Figure 5 adds confidence to our interpretations as it demonstrates good agreement between the simulated and measured wind profiles for the strongly forced conditions observed in the laboratory experiment [2]. As wave age increases, the overlying wind profiles for the incipient and active breakers "feel" the reduction in surface form stress. Notice the wind profiles systematically shift to the right at all values of ζ for increasing c/u_*. This wind speed up is indicative of an overall decrease in total surface drag resulting from a decrease in form drag. For the same steep geometrical waveshape, the underlying wave surface appears effectively smoother when the wave train propagates rapidly with $c/u_* = 10$ compared to when it propagates slowly with $c/u_* \sim 1$.

4. Discussion and summary

Unsteady flow separation impacts numerous applications and continues to be an active area of boundary-layer research, *e.g.,* [8, 6, 13]. While the onset of laminar flow separation over a stationary 2-D wall is accurately defined by the surface shear stress = 0 criterion, no similarly simple rule exists for unsteady turbulent flow over moving walls. For unsteady regimes, theoretical models often adopt the so-called Moore-Rott-Sears criterion, *i.e.,* flow separation over a moving wall requires that the velocity profile has simultaneously zero velocity and shear in a frame of reference moving with the separation point, for example see Fig. 1 in [8] and discussion in [4, 6, 13]. Also, with moving boundaries the location of flow separation occurs in the outer flow away from the surface. Results from physical modeling find wall movement progressing in the freestream direction delays flow separation while wall movement opposite to the freestream advances flow separation. Wall movement is then a technique for active flow separation control in engineering flows, *e.g.,* flow past an airfoil with a rotating leading edge [8].

The large-eddy simulations of turbulent flow over steep steady and unsteady wave trains described here display features similar to their counterparts in engineering flows with moving walls. At low wave age the overlying winds are moving rapidly compared to the slow vertical oscillations of the wave boundary, and analysis of LES solutions finds flow separation on the leeward side of the wave which results in large pressure drag. In this low wave age regime, simulation results [17] for incipient and active breakers are in good agreement with measured wind profiles and form (pressure) drag reported in the literature. The simulations further emphasize the importance of waveslope under strongly forced conditions. Increases in wave age produce an order unity change in the flow dynamics over steep waves. For the same geometrical waveshape, as c/u_* increases the speed of the vertical oscillations of the wave boundary intensify, they are proportional to the wave speed and local waveslope. Because the waveslope is asymmetrical about the wave crest, the forward boundary movement is a maximum on the leeward side of a propagating wave. The boundary movement can then delay or erase flow separation leading to a sharp decrease in form drag. For example, with the active breaker case the pressure drag is nearly 75% of the total drag when $c/u_* = 1.23$ but falls to less than 20% when $c/u_* = 10$. The impact of wave age on flow separation described here appears to be generic for steep steady and unsteady wave trains. Over the range of wave age considered the critical layer height h_{cr} above the waves is confined to a very thin region near the wave surface and its role in turbulent flow over steep waves is not fully understood [12, 16]. In turbulent flow over monochromatic waves with $ak < 0.1$ and no separation [20] a near surface critical layer causes the drag to increase. The simulations described here are highly idealized, but pose potentially interesting observational questions for a field of steep waves at high winds in the open ocean. When does flow separation occur and if so at what scale, what is the role of a critical layer for a spectrum of waves, and what is the role of wave unsteadiness in setting the surface drag.

Acknowledgements

This work was supported by the Office of Naval Research through the Physical Oceanography Program. PPS was supported by award numbers N00014-13-G-0223-0002, N00014-14-1-0626, N00014-17-1-2334, and the National Science Foundation through the National Center for Atmospheric Research (NCAR). MLB, RPM and WLP acknowledge support from award number N00014-12-10184. This research benefited greatly from computer resources provided by the NCAR Strategic Capability program managed by the NCAR Computational Information Systems Laboratory, http://n2t.net/ark:/85065/d7wd3xhc, and the Department of Defense High Performance Computing Modernization Program.

References

1. Alves, J.G.M., Banner, M.L., Young, I.R., 2003. Revisiting the Pierson-Moskowitz asymptotic limits for fully developed wind waves. J. Phys. Oceanogr. 33, 1301–1323.
2. Banner, M.L., 1990. The influence of wave breaking on the surface pressure distribution in wind-wave interaction. J. Fluid Mech. 211, 463–495.
3. Barthelemy, X., Banner, M.L., Peirson, W.L., Fedele, F., Allis, M., , Dias, F., 2018. On a unified breaking onset threshold for gravity waves in deep and intermediate depth water. J. Fluid Mech. in press.
4. Belcher, S.E., Hunt, J.C.R., 1998. Turbulent flow over hills and waves. Annu. Rev. Fluid Mech. 30, 507–538.
5. Buckley, M.P., Veron, F., 2016. Structure of the airflow above surface waves. J. Phys. Oceanogr. 46, 1377–1397.

6. Degani, A.T., Walker, J.D.A., Smith, F.T., 1998. Unsteady separation past moving surfaces. J. Fluid Mech. 375, 1–38.
7. Edson, J., Crawford, T., Crescenti, J., Farrar, T., French, J., Frew, N., Gerbi, G., Helmis, C., Hristov, T., Khelif, D., Jessup, A., Jonsson, H., Li, M., Mahrt, L., McGllis, W., Plueddmann, A., Shen, L., Skyllingstad, E., Stanton, T., Sullivan, P., Sun, J., Trowbridge, J., Vickers, D., Wang, S., Wang, Q., Weller, R., Wilkin, J., Yue, D., Zappa, C., 2007. The coupled boundary layers and air-sea transfer experiment in low winds (CBLAST-Low). Bull. Amer. Meteorol. Soc. 88, 342–356.
8. Gad-el-Hak, M., Bushnell, D.M., 1991. Separation control: Review. Journal of Fluids Engineering 113, 19–30.
9. Grare, L., Lenain, L., Melville, W., 2013. Wave-coherent airflow and critical layers over ocean waves. J. Phys. Oceanogr. 43, 2156–2172.
10. Hara, T., Sullivan, P.P., 2015. Wave boundary layer turbulence over surface waves in a strongly forced condition. J. Phys. Oceanogr. 45, 868–883.
11. Hristov, T., Miller, S.D., Friehe, C., 2003. Dynamical coupling of wind and ocean waves through wave-induced air flow. Nature 422, 55–58.
12. Miles, J.W., 1957. On the generation of surface waves by shear flow, Part I. J. Fluid Mech. 3, 185–204.
13. Miron, P., Vétel, J., 2015. Towards the detection of moving separation in unsteady flows. J. Fluid Mech. 779, 819–841.
14. Phillips, O.M., 1977. Dynamics of the Upper Ocean. Cambridge University Press.
15. Reul, N., Branger, H., Giovanangeli, J.P., 2007. Air flow structure over short-gravity breaking waves. Boundary-Layer Meteorol. 126, 477–505.
16. Sajjadi, S.G., Hunt, J.C.R., Drullion, F., 2014. Asymptotic multi-layer analysis of wind over unsteady monochromatic surface waves. J. of Engineering Mathematics 84, 73–85.
17. Sullivan, P.P., Banner, M.L., Morisson, R.P., Peirson, W.L., 2018. Turbulent flow over steep steady and unsteady waves under strong wind forcing. J. Phys. Oceanogr. 48, 3–27.
18. Sullivan, P.P., Edson, J.B., Hristov, T., McWilliams, J.C., 2008. Large eddy simulations and observations of atmospheric marine boundary layers above non-equilibrium surface waves. J. Atmos. Sci. 65, 1225–1245.
19. Sullivan, P.P., McWilliams, J.C., 2010. Dynamics of winds and currents coupled to surface waves. Annu. Rev. Fluid Mech. 42, 19–42.
20. Sullivan, P.P., McWilliams, J.C., Moeng, C.H., 2000. Simulation of turbulent flow over idealized water waves. J. Fluid Mech. 404, 47–85.
21. Sullivan, P.P., McWilliams, J.C., Patton, E.G., 2014. Large eddy simulation of marine boundary layers above a spectrum of moving waves. J. Atmos. Sci. 71, 4001–4027.
22. Veron, F., Saxena, G., Misra, S.K., 2007. Measurements of the viscous tangential stress in the airflow above wind waves. Geophys. Res. Lett. 34. L19603.